Liu *et al. Energy Mater.* **2025**, *5*, 500094
DOI: 10.20517/energymater.2024.308

Energy Materials

Article

Open Access

Check for updates

Constructing an enhanced charge-mass transfer passage for silicon anodes to achieve increased capacity under high-rate conditions

Jifei Liu[1,2,*], Yongzhi Wan[1], Kefeng Wang[1], Kai Wang[1,2], Wanjun Sun[1,2], Jianfeng Dai[3], Zengpeng Li[4,*], Feitian Ran[1,2,*]

[1]School of New Energy and Power Engineering, Lanzhou Jiaotong University, Lanzhou 730070, Gansu, China.
[2]Power Battery Technology Innovation Center of Gansu Province, Jinchang 737100, Gansu, China.
[3]School of Science, State Key Laboratory of Advanced Processing and Recycling of Nonferrous Metals, Lanzhou University of Technology, Lanzhou 730050, Gansu, China.
[4]Key Laboratory of Solar Power System Engineering, Jiuquan Vocational and Technical College, Jiuquan 735000, Gansu, China.

[*]**Correspondence to:** Assoc. Prof. Jifei Liu and Assoc. Prof. Feitian Ran, School of New Energy and Power Engineering, Lanzhou Jiaotong University, 88 Anning West Rd., Anning District, Lanzhou 730070, Gansu, China. E-mail: liujifei@mail.lzjtu.cn; ranft@lzjtu.edu.cn; Prof. Zengpeng Li, Key Laboratory of Solar Power System Engineering, Jiuquan Vocational and Technical College, 64 Jiefang Rd., Suzhou District, Jiuquan 735000, Gansu, China. E-mail: lzpjqzy@163.com

How to cite this article: Liu, J.; Wan, Y.; Wang, K.; Wang, K.; Sun, W.; Dai, J.; Li, Z.; Ran, F. Constructing an enhanced charge-mass transfer passage for silicon anodes to achieve increased capacity under high-rate conditions. *Energy Mater.* **2025**, *5*, 500094. https://dx.doi.org/10.20517/energymater.2024.308

Received: 31 Dec 2024 **First Decision:** 26 Jan 2025 **Revised:** 15 Feb 2025 **Accepted:** 25 Feb 2025 **Published:** 28 Apr 2025

Academic Editor: Jiaqi Huang **Copy Editor:** Ping Zhang **Production Editor:** Ping Zhang

Abstract

Silicon (Si) holds promise as an anode material for next-generation lithium-ion batteries due to its high theoretical capacity. However, practical applications are impeded by structural damage from volume expansion. Here, we designed a novel Si/CNFs/C anode by integrating mesoporous Si particles, carbon nanofibers (CNFs), and carbon quantum dots into a three-dimensional (3D) architecture via a one-step magnesiothermic reduction process. This design significantly enhances both electron and ion conductivity, alleviates the volume expansion of Si particles, and ensures mechanical stability during battery operation. Consequently, batteries with the Si/CNFs/C anode exhibit a reversible capacity of 1,172.4 mAh g^{-1} after 200 cycles at 0.1 A g^{-1} and maintain 1,107.7 mAh g^{-1} after 1,000 cycles at 1 A g^{-1}. Notably, after 1,000 cycles at a high current density of 1 A g^{-1}, the capacity remains nearly comparable to that after 100 cycles at 0.1 A g^{-1}, attributed to significant pseudocapacitive characteristics that facilitate high performance under elevated current densities. Furthermore, we employed distribution of relaxation times analysis alongside other electrochemical techniques to investigate changes in ion transport pathways and the evolving role of Si in the energy storage process. Our design and analysis provide valuable insights for optimizing

3D conductive architectures and understanding the dynamic electrochemical mechanisms of Si-based anodes, advancing the development of high-performance lithium-ion batteries.

Keywords: Silicon anodes, lithium-ion batteries, carbon nanofibers, carbon quantum dots, three-dimensional architecture, electrochemical performance

INTRODUCTION

The selection of anode material is fundamental to shaping the energy density, cycling stability, and overall electrochemical performance of lithium-ion batteries, as it directly governs key processes such as ion storage, charge transport, and structural integrity during cycling. Silicon (Si) has emerged as a leading candidate for next-generation lithium-ion battery anodes, attributed to its extraordinarily high theoretical capacity of 4,200 mAh g^{-1}, low operating potential (~0.37 V *vs.* Li/Li^+), and natural abundance, which collectively present immense potential for enhancing energy density[1]. Despite these advantages, its practical implementation is significantly constrained by a severe volume expansion (~400%) during lithiation and delithiation, resulting in structural pulverization, rapid capacity decay, and poor electrical conductivity that impedes efficient electron transport[2]. Overcoming these intrinsic challenges is critical to fully leveraging the benefits of Si and advancing the development of high-performance lithium-ion battery technologies[3].

To mitigate the challenges associated with Si anodes, integrating Si with carbon materials has emerged as an effective strategy[4-6]. Zhou *et al.* achieved a sustainable high-capacity Si anode by implementing a dual-layer interface architecture that integrates an internal SiO_x layer with an external N, B co-doped carbon coating, accommodating the volumetric changes of Si during cycling and establishing robust pathways for ion and electron transport, thereby significantly enhancing the stability and electrochemical performance of the anode[7]. Similarly, Han *et al.* enhanced electrical conductivity and mitigated stress by designing a hierarchical submicron Si-carbon architecture that incorporates nanoscale Si particles within a conductive carbon matrix, thereby establishing resilient conductive networks and effectively accommodating the volumetric expansion of Si during charge-discharge cycles[8]. Collectively, these studies have significantly improved cycling stability and rate performance, thereby advancing the development of Si anodes.

Despite these encouraging advances, Si-based anodes still face fundamental hurdles, including disrupted conduction pathways and sluggish electrochemical kinetics, which lead to uneven lithium-ion distribution, heightened polarization, and ultimately diminished rate capability[9,10]. An optimized structural design is therefore essential to fully harness the high theoretical capacity of Si. Specifically, three key elements are crucial: (i) structural modification of Si to introduce ion diffusion channels and address slow kinetics, (ii) incorporation of conductive networks to enhance electron transport and suppress volume expansion, and (iii) design of mass transport pathways to enable efficient ion and electron movement from external carbon to the interior of Si[11-15]. Guided by these principles, our approach introduces ion diffusion channels, robust conductive frameworks, and optimized mass transport routes to collectively improve electrochemical performance and extend the operational lifespan of anodes.

Building on this framework, the present study proposes a novel structural optimization by developing a Si/carbon nanofibers (CNFs)/C composite to address the aforementioned challenges. This composite is synthesized via a one-step magnesiothermic reduction that creates three-dimensional (3D) conductive pathways, thereby enhancing electrochemical performance and cycle stability. During fabrication, Si inherits the mesoporous architecture of dendritic mesoporous SiO_2, forming internal ion diffusion channels that alleviate sluggish ion transport issues. Additionally, carbon quantum-derived carbon (CQDs-C) and CNFs

collectively establish a robust conductive network: the small size of carbon quantum dots (CQDs) allows them to penetrate the pores of Si particles and generate in situ carbon layers, seamlessly linking internal Si surfaces to external carbon. This continuous conductive framework not only promotes electron transport but also provides mechanical support to accommodate the volumetric changes of Si. To prevent agglomeration, NaCl serves as both a thermal conductor and pore-forming agent, generating favorable porous structures within the composite and facilitating efficient ion-electron movement. Notably, the resulting Si/CNFs/C anode exhibits an intriguing upward trend in electrochemical performance that gradually stabilizes over prolonged cycling. To clarify this observation, we combined distribution of relaxation times (DRT) with a series of electrochemical techniques to investigate changes in ion transport pathways and the evolving role of Si in the energy storage process.

EXPERIMENTAL

Synthesis of samples

Materials

All reagents and chemicals were obtained from Shanghai Macklin Biochemical Co., Ltd. (Shanghai, China) and used as received, without any further purification.

Synthesis of carbon quantum dots

CQDs were synthesized using a microwave-assisted method. Initially, 5 g of citric acid and 5 g of urea were thoroughly dissolved in 20 mL of deionized water with continuous stirring to form a uniform solution. This homogeneous mixture was then subjected to microwave heating at a power level of 1,100 W for 5 min using a standard household microwave oven. After microwave irradiation, the mixture was allowed to cool to room temperature, resulting in the formation of a black solid residue. This solid was collected and vacuum-dried at 80 °C for 1 h to remove any residual moisture. The dried material was subsequently re-dispersed in 30 mL of deionized water and centrifuged to eliminate large particulate aggregates. The clear supernatant, containing the dark brown CQDs suspension, was carefully separated and freeze-dried to obtain a fine brown CQDs powder.

Synthesis of carbon nanofibers

CNFs were synthesized via electrospinning, followed by thermal stabilization and carbonization. Polyacrylonitrile (PAN) (1 g) was dissolved in 10 mL of N, N-dimethylformamide (DMF) and stirred at room temperature for 24 h to achieve complete dissolution. The solution was then sonicated for 30 min to remove any air bubbles. The PAN solution was loaded into a syringe fitted with a flat-head needle and electrospun under controlled conditions to form uniform nanofibers. The collected nanofibers were vacuum-dried at 60 °C for 6 h to eliminate the residual solvent. The dried mats were then thermally stabilized at 260 °C for 3 h in the air to induce cyclization and aromatization. Finally, the stabilized fibers were carbonized in an argon atmosphere at 800 °C, with a heating rate of 2 °C min^{-1}, for 2 h to yield CNFs.

Synthesis of Si/CNFs/C, Si/CNFs, and Si/C composites

The Si/CNFs/C, Si/CNFs, and Si/C composites were prepared via magnesiothermic reduction of SiO_2 nanoparticles, as detailed in our previous publication[13]. For the synthesis of Si/CNFs/C, a mixture of 0.6 g of SiO_2, 0.1 g of CQDs, 0.1 g of CNFs, and 0.6 g of NaCl was ground in an agate mortar until homogeneous. In this process, NaCl acted as both a dispersing agent to prevent particle agglomeration and a thermal conductor to promote uniform heat distribution during the reduction. The mixture was then blended with 0.6 g of magnesium powder, which served as the reducing agent. The resulting blend was placed in a tube furnace and subjected to magnesiothermic reduction at 650 °C for 6 h under an argon atmosphere to prevent oxidation. After cooling to room temperature, the product was washed sequentially with 1 mol L^{-1}

hydrochloric acid (HCl) and 4% hydrofluoric acid (HF) to remove residual magnesium, MgO, Mg_2Si, and unreacted SiO_2. The sample was then rinsed with deionized water until the pH reached neutral. To eliminate residual moisture, the product was vacuum-dried at 60 °C for 12 h. For comparison, Si/CNFs and Si/C composites were synthesized under identical conditions, excluding the addition of CQDs and CNFs, respectively, to assess the individual contributions of these components to the composite properties.

Characterization

The phase composition and crystal structure of the synthesized samples were examined using X-ray diffraction (XRD) on a LabRAM HR800 diffractometer with Cu Kα radiation (λ = 0.15418 nm). The scans were conducted over a 2θ range of 20° to 70° with a step size of 0.02° and a scan rate of 6° min^{-1}, providing detailed information on the crystalline phases. The surface morphology and microstructure were characterized by scanning electron microscopy (SEM, Zeiss Gemini 500) and transmission electron microscopy (TEM, JEM-F200). Elemental composition and distribution were further analyzed using energy-dispersive X-ray spectroscopy (EDS) mapping via a JED-2300T detector integrated with the TEM, enabling high-resolution elemental imaging. Raman spectroscopy (LabRAM HR800, Horiba Jobin Yvon) with a 532 nm excitation wavelength was used to examine the bonding characteristics and structural properties of the carbon and silicon phases. The surface chemical states of the products were analyzed using X-ray photoelectron spectroscopy (XPS) with an Axis Supra instrument, operated at 150 W and 10 mA, utilizing a monochromatic Al Kα X-ray source for two scan cycles. Nitrogen adsorption-desorption measurements were carried out using the Brunauer-Emmett-Teller (BET) method (TRISTAR 3000 analyzer) to determine the specific surface area and pore size distribution, revealing crucial porosity characteristics relevant to electrochemical performance. The carbon content and thermal stability were assessed via thermogravimetric analysis (TGA) on a PerkinElmer TGA 8000 instrument. The TGA measurements were performed from room temperature to 1,000 °C at a heating rate of 10 °C min^{-1} under controlled conditions to evaluate weight loss corresponding to carbon decomposition and oxidation.

Electrochemical measurement

The working anodes were prepared by mixing the active material, conductive carbon black (Super P), and sodium carboxymethyl cellulose (CMC) binder in a 7:2:1 mass ratio using deionized water to form a uniform slurry. The slurry was coated onto copper foil and dried at 80 °C for 12 h to eliminate residual moisture, achieving active material mass loadings of 0.76 mg cm^{-2} for Si/CNFs/C, 0.648 mg cm^{-2} for Si/CNFs, and 0.87 mg cm^{-2} for Si/C. Electrochemical tests were conducted on CR2025 coin cells assembled in an argon-filled glovebox, with lithium metal foil as both the counter and reference electrode and a Celgard 2400 membrane as the separator. The electrolyte consisted of 1 M $LiPF_6$ dissolved in a 1:1:1 mixture of ethylene carbonate (EC), diethyl carbonate (DEC), and dimethyl carbonate (DMC). Cyclic voltammetry (CV) was performed using a CHI 760E electrochemical workstation at a scan rate of 0.1 mV s^{-1} over a voltage window of 0-3 V (*vs.* Li/Li^+) to evaluate electrochemical reactions and reversibility. Electrochemical impedance spectroscopy (EIS) was conducted by applying a 10 mV alternating current (AC) voltage over a 100 kHz-0.01 Hz frequency range to analyze charge transfer resistance (R_{ct}) and ion diffusion behavior. The DRT technique further deconvoluted the EIS spectra at different voltages within the same range, revealing insights into individual electrochemical processes. Galvanostatic charge-discharge (GCD) tests and cycling performance measurements were conducted using a LAND battery testing system within a voltage range of 0.01-3 V (*vs.* Li/Li^+). To determine lithium-ion diffusion coefficients (D_{Li^+}), galvanostatic intermittent titration technique (GITT) tests were performed by applying a constant current pulse for 30 min, followed by a 120 min open-circuit relaxation period to allow the system to equilibrate. By carefully controlling the anode preparation and testing conditions, reliable and reproducible electrochemical data were obtained to evaluate the performance of the synthesized composites.

Calculation method

Spin-polarized density functional theory (DFT) calculations were performed using plane-wave basis sets and the projector augmented-wave (PAW) method. The exchange-correlation functional was treated using the generalized gradient approximation (GGA) with the Perdew-Burke-Ernzerhof (PBE) parameterization. An energy cutoff of 400 eV was set for the calculations. The Brillouin-zone integration was carried out using a Γ-centered Monkhorst-Pack grid of 1 × 1 × 1, with the sampling process handled by VASPKIT. The system was fully relaxed until the maximum force on each atom was less than 0.1 eV/Å, and the energy convergence criterion was set to 10^{-4} eV. Van der Waals interactions were included using the DFT-D3 correction proposed by Grimme. To prevent periodic interactions in the interface structures, a vacuum layer of 15 Å was added along the c-axis, perpendicular to the interface.

RESULT AND DISCUSSION

To address the inherent challenges of Si anodes, including poor conductivity and significant volumetric expansion during cycling, we designed a novel strategy based on a one-step magnesiothermic reduction process [Scheme 1]. This approach enabled the successful fabrication of a Si/CNFs/C composite with 3D conductive pathways, exhibiting exceptional electrochemical performance. The method effectively addresses the key limitations of Si, providing a robust solution for improving cycling stability and rate capability[16].

In this synthesis, the Si particles inherit the mesoporous structure of the dendritic SiO_2 precursor, which plays a vital role in forming internal ion diffusion channels. These channels effectively reduce ion transport resistance, a common challenge in traditional Si-based anodes, thereby significantly enhancing the anode's electrochemical kinetics[17]. The SEM image of the SiO_2 precursor [Figure 1A] reveals a well-defined dendritic mesoporous structure, offering a highly accessible porous framework essential for facilitating efficient ion diffusion. Additionally, the inset TEM image confirms the presence of continuous internal pores extending from the interior to the surface. During the magnesiothermic reduction process, this porous architecture is preserved in the Si particles, further improving ion transport and enhancing electrochemical performance[18]. Figure 1B-C shows SEM images of the synthesized Si/CNFs/C composite, which features a network-like morphology with interwoven CNFs forming a 3D porous architecture. Employing NaCl as a pore-forming agent effectively fosters the formation of this porous architecture while preventing particle agglomeration[19]. For comparison, Si/CNFs and Si/C anodes were also prepared using similar methods, as illustrated in Supplementary Figure 1. The small size of the CQDs allows them to penetrate into the mesoporous Si structures, generating carbon layers in situ on the inner walls of the Si pores [Figure 1D]. This process leads to the formation of an interpenetrating 3D conductive network that connects the external carbon matrix to the internal Si particles, which is critical for facilitating both ion diffusion and electron transport, thereby enhancing electrochemical kinetics[20,21]. The two-dimensional carbon layers derived from CQDs and the one-dimensional CNFs form a robust, interconnected conductive network that promotes electron transport and maintains structural integrity. This hierarchical structure of the composite is demonstrated in the TEM image [Figure 1E], which shows the interconnection of the carbon layers and CNFs. The selected area electron diffraction (SAED) pattern [Figure 1F] further confirms the crystalline nature of the Si phase by exhibiting distinct diffraction rings characteristic of crystalline Si, supporting the successful reduction of SiO_2 to Si. The high-resolution TEM (HRTEM) image [Figure 1G] displays clear lattice fringes with a spacing of 0.31 nm, corresponding to the (111) crystal plane of crystalline Si, further confirming the crystalline nature of Si in the composite and verifying the successful transformation of SiO_2 to Si. Elemental mapping images [Figure 1H] demonstrate the homogeneous distribution of Si and carbon within the composite. The Si particles are uniformly embedded within the carbon matrix, with CNFs interwoven throughout the network. Together, the CNFs and CQDs-C form a continuous 3D structure that encapsulates the Si particles, enhancing electron transport and providing mechanical support to the composite, thereby greatly improving its electrochemical performance.

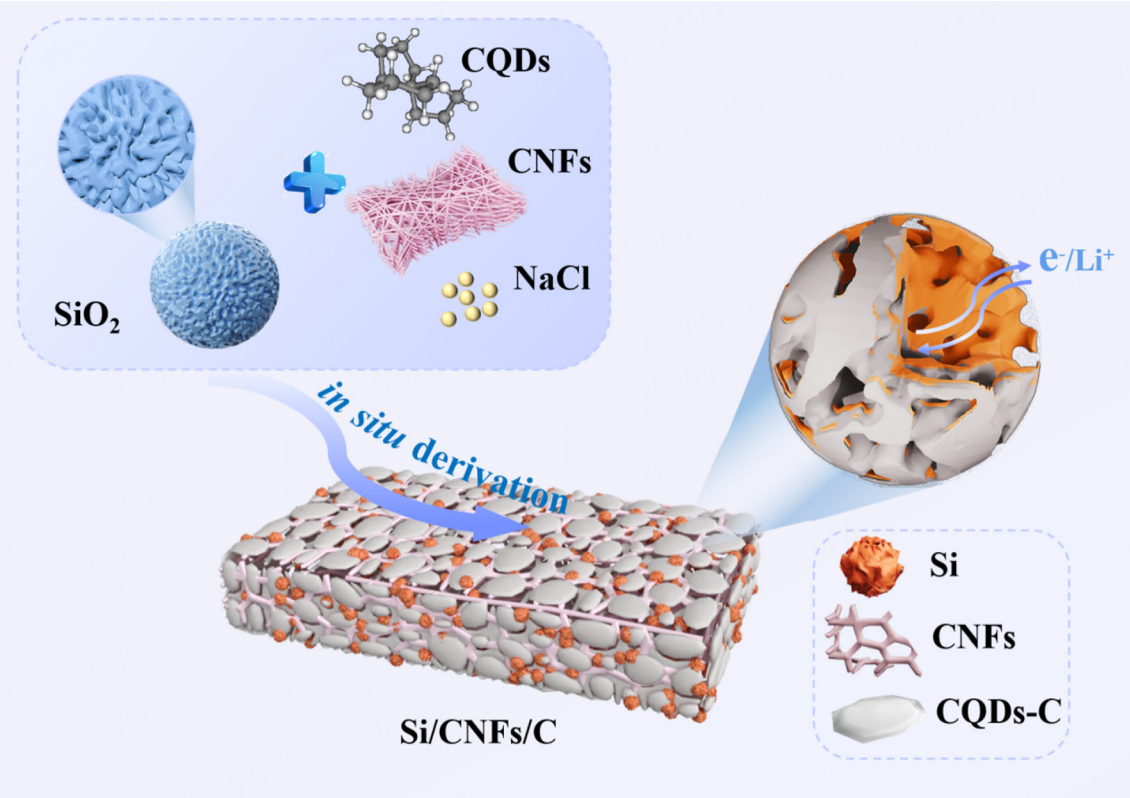

Scheme 1. Schematic illustration of the one-step magnesiothermic reduction process for synthesizing the Si/CNFs/C composite. CNFs: Carbon nanofibers; CQDs-C: carbon quantum-derived carbon.

XRD analysis, as shown in Figure 2A, was performed to explore the structural properties of the synthesized materials. After magnesiothermic reduction and subsequent HF washing to remove residual by-products, distinct diffraction peaks at 28.4°, 47.3°, 56.1°, and 69.1° were observed, corresponding to the (111), (220), (311), and (400) planes of crystalline Si (JCPDS No. 27-1402), indicating that the SiO_2 in the composite was effectively reduced to Si[13]. To further investigate the composition and thermal stability of the samples, TGA was conducted, and the results are presented in Figure 2B. The TGA curves show three distinct stages, representing the evaporation of residual water, the oxidation of Si, and the combustion of carbon, respectively[22]. Based on the TGA data, the Si content in the Si/C, Si/CNFs, and Si/CNFs/C composites was determined to be 72.9%, 76.8%, and 63.2%, respectively. To assess the porosity and surface area of the Si/CNFs/C composite, nitrogen (N_2) adsorption-desorption isotherms were measured, as depicted in Figure 2C. The isotherms displayed an H2-type hysteresis loop, characteristic of mesoporous structures, confirming the presence of mesoporosity in the material. The specific surface area was found to be 196.9 m^2/g, suggesting significant surface area available for electrochemical reactions. The pore size distribution, derived from the desorption branch of the isotherm, revealed two distinct pore sizes of approximately 3.7 nm and 19.2 nm. The smaller pore size (3.7 nm) is attributed to the mesoporous silica precursor, enhancing ion diffusion, while the larger pore size (19.2 nm) is likely formed during the magnesiothermic reduction process[14,18]. Figure 2D shows the Raman spectra of Si/CNFs/C, Si/CNFs, and Si/C, with peaks at 293.4 cm^{-1}, 516.2 cm^{-1}, and 938.4 cm^{-1} corresponding to crystalline Si. Two prominent peaks are observed around 1,334.1 cm^{-1} and 1,594.3 cm^{-1}, which are attributed to the D and G bands of carbon after heat treatment. The area percentages of the D and G peaks provide insight into the degree of disorder in the carbon structure of the composites[19]. For Si/CNFs/C, the I_D/I_G ratio is 0.77, while for Si/CNFs, it is 0.720. Si/C exhibits a significantly higher I_D/I_G ratio of 1.58. These results indicate that the

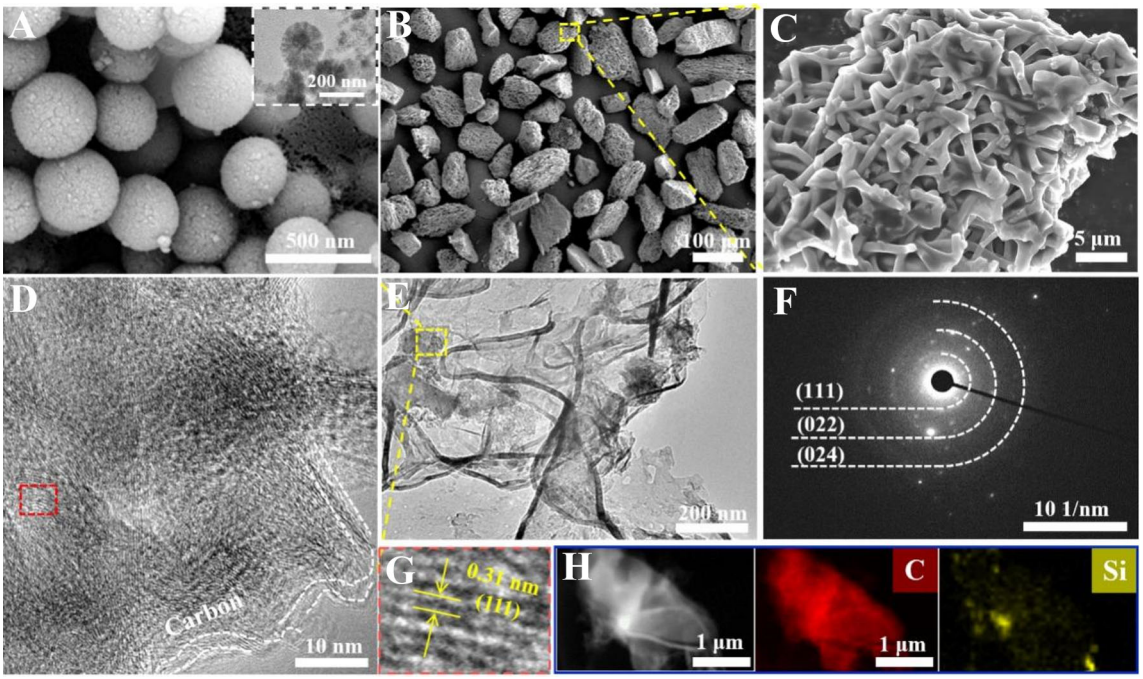

Figure 1. (A) SEM image of the SiO_2 precursor; inset: TEM image of SiO_2; Morphology and compositional analysis of the Si/CNFs/C composite: (B and C) SEM images at low and high magnifications; (D and E) TEM images at varying magnifications; (F) Selected area electron diffraction (SAED) pattern; (G) High-resolution TEM (HRTEM) image; (H) Elemental mapping. SEM: Scanning electron microscopy; TEM: transmission electron microscopy.

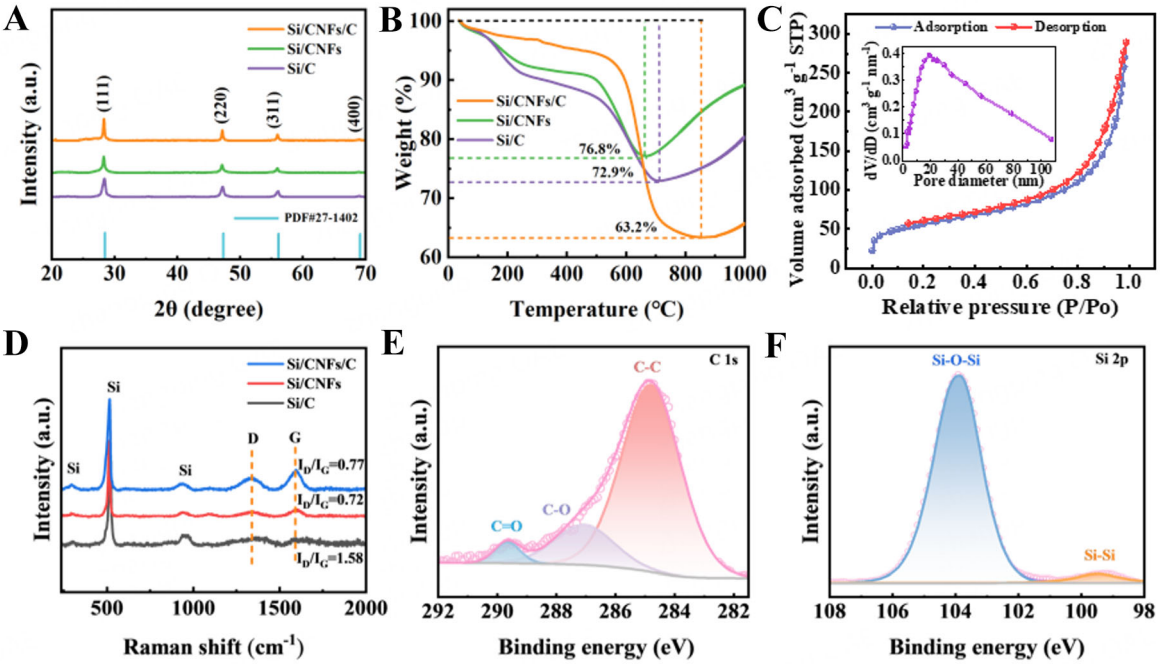

Figure 2. (A) XRD patterns of Si/C, Si/CNFs, and Si/CNFs/C composites; (B) TGA curves of Si/C, Si/CNFs, and Si/CNFs/C composites; (C) N_2 adsorption-desorption isotherms of the Si/CNFs/C composite; (D) Raman spectra of Si/C, Si/CNFs and Si/CNFs/C composites; (E) C 1s and (F) Si 2p XPS spectrum of the Si/CNFs/C. CNFs: Carbon nanofibers; XRD: X-ray diffraction; TGA: thermogravimetric analysis; XPS: X-ray photoelectron spectroscopy.

carbon in Si/C has a much higher defect density and lower graphitization compared to the carbon in Si/CNFs and Si/CNFs/C. The relatively lower I_D/I_G ratios in Si/CNFs and Si/CNFs/C suggest a higher degree of graphitization, which is beneficial for electrical conductivity and overall electrochemical performance. The slightly higher I_D/I_G ratio in Si/CNFs/C compared to Si/CNFs may be attributed to the incorporation of CQDs, which introduce some additional defects, yet still contribute positively to the composite's conductivity and interface properties. In addition, XPS revealed the surface chemical properties of Si/CNFs/C. The full spectrum [Supplementary Figure 2] clearly displayed characteristic peaks for O 1s, C 1s, Si 2s, and Si 2p, indicating the presence of O, C, and Si elements. The high-resolution C 1s spectrum of Si/CNFs/C [Figure 2E] shows three sub-peaks at 284.8 eV (C-C), approximately 286.4 eV (C-O), and 288.8 eV (C=O). In the high-resolution Si 2p XPS spectrum shown in Figure 2F, the peak fitting at 99.5 eV corresponds to the Si-Si bond, while the peak at 103.9 eV is associated with Si-O-Si bonds related to SiO_2. The higher intensity of the SiOx-related peak can be attributed to the thin SiO_2 layer formed on the surface of Si due to oxidation when exposed to air. However, due to the limited detection depth of XPS, which primarily analyzes the surface layer, the SiO_2 peak is more prominent. Based on the XRD and Raman data, the proportion of SiO_2 in Si/CNFs/C is still much smaller than that of Si. Furthermore, the Si-O-C bond contributes to the strong bonding between Si and the amorphous carbon layer, and the presence of a small amount of SiO_2 helps maintain the structure of Si/CNFs/C during cycling[16].

To evaluate the electrochemical behavior of Si/C, Si/CNFs, and Si/CNFs/C composite anodes, CV tests were performed at a scan rate of 0.5 mV s^{-1}, as illustrated in Figure 3A. For the Si/CNFs/C composite, three reduction peaks appear in the first cathodic sweep, located around 1.42 V, 0.26 V, and 0.12 V. These peaks are attributed to Li^+ storage within the carbon matrix, the formation of the solid electrolyte interphase (SEI), and the subsequent alloying reaction producing Li_xSi phases, respectively. During the anodic sweep, a distinct peak emerges at approximately 1.24 V, corresponding to the extraction of Li^+ ions from the carbon matrix. In subsequent cycles, the redox behavior stabilizes, exhibiting a reduction peak at ~0.85 V and an oxidation peak near 1.24 V, indicating the reversible insertion/extraction of Li^+. For comparison, the CV curves of Si/C and Si/CNFs anodes are provided in Supplementary Figure 3, respectively. The Si/C and Si/CNFs anodes exhibit similar electrochemical processes, with oxidation peaks observed at 0.36 V and 0.53 V for Si/C, and 0.38 V and 0.53 V for Si/CNFs, which are characteristic of the Li_xSi phase dealloying. Notably, the Si/CNFs/C composite exhibits unique oxidation behavior, where a single oxidation peak appears in each of the initial three cycles. This peak shifts progressively from 0.37 V in the first cycle to 0.54 V in the second and 0.46 V in the third, likely linked to the gradual dealloying of Li_xSi phases. To further investigate the cycling performance, GCD tests were carried out at a current density of 0.1 A g^{-1}, as depicted in Figure 3B. After 200 cycles, the Si/CNFs/C anode retained a specific capacity of 1,172.4 mAh g^{-1}, which significantly exceeds the performance of Si/CNFs (604.1 mAh g^{-1}) and Si/C (399.4 mAh g^{-1}) anodes. This enhanced cycling stability is credited to the synergistic contributions of CNFs and the CQDs-C, which together provide robust mechanical reinforcement and superior electronic conductivity. Such features effectively mitigate the volume expansion typically encountered in Si-based anodes[22].

Figure 3C demonstrates the rate performance of the Si/C, Si/CNFs, and Si/CNFs/C anodes over a range of current densities (0.1 A g^{-1} to 5 A g^{-1}). The Si/CNFs/C anode exhibits exceptional rate capability, delivering specific capacities of 1,062.2 mAh g^{-1}, 1,013.3 mAh g^{-1}, 870.6 mAh g^{-1}, 788.6 mAh g^{-1}, and 698.8 mAh g^{-1} at current densities of 0.1 A g^{-1}, 0.2 A g^{-1}, 0.5 A g^{-1}, 1 A g^{-1}, and 2 A g^{-1}, respectively. Even at a high current density of 5 A g^{-1}, it maintains a notable capacity of 582 mAh g^{-1}. When the current density is reduced back to 0.1 A g^{-1}, the capacity quickly recovers to 1,191.3 mAh g^{-1}, which is nearly identical to the second cycle's value at the same current density. The GCD profiles of the Si/CNFs/C anode at various current densities, presented in Figure 3D, indicate minimal capacity decay with increasing current density from 0.1 A g^{-1} to

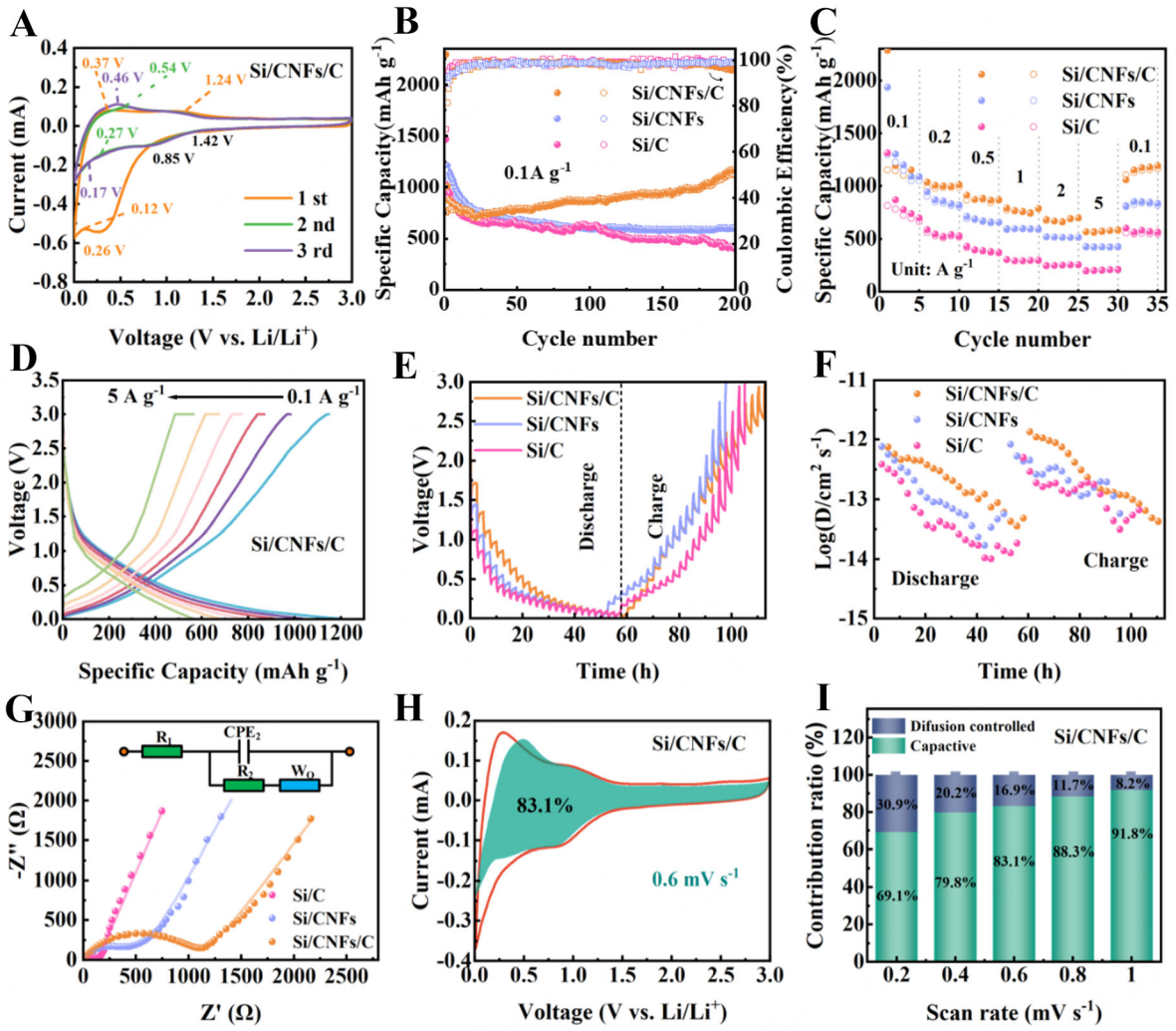

Figure 3. (A) CV curves of the Si/CNFs/C anode during the first three cycles; (B) Cycling performance of Si/C, Si/CNFs, and Si/CNFs/C anodes; (C) Rate capability of the three anodes; (D) GCD profiles of the Si/CNFs/C anode at different current densities; (E) GITT curves of Si/C, Si/CNFs, and Si/CNFs/C anodes; (F) Calculated lithium-ion diffusion coefficients for Si/C, Si/CNFs, and Si/CNFs/C anodes; (G) Nyquist plots of fresh Si/C, Si/CNFs, and Si/CNFs/C anodes; (H) Pseudocapacitive contribution of the Si/CNFs/C anode at a scan rate of 0.6 mV s^{-1}; (I) Pseudocapacitive contributions of the Si/CNFs/C anode at various scan rates. CV: Cyclic voltammetry; CNFs: carbon nanofibers; GCD: galvanostatic charge-discharge; GITT: galvanostatic intermittent titration technique.

5 A g^{-1}. By comparison, the Si/CNFs and Si/C anodes achieve capacities of 513.4 mAh g^{-1} and 254.5 mAh g^{-1} at 5 A g^{-1}, respectively. Although these values are lower than that of the Si/CNFs/C anode, they remain significant. Interestingly, while the Si/C anode demonstrates a lower overall capacity than the Si/CNFs anode, it shows better capacity retention, as evidenced in Supplementary Figure 4.

To analyze the exceptional electrochemical performance of the Si/CNFs/C composite from the perspective of reaction kinetics, GITT measurements were carried out on all three anodes, as shown in Figure 3E. The lithium-ion diffusion behavior was evaluated using the logarithmic form of the diffusion coefficient (log *D*), which can be derived from

$$D=\frac{4L^2}{\pi\tau}\left(\frac{\Delta E_s}{\Delta E_\tau}\right)^2 \quad (1)$$

where L is the diffusion length of the lithium ion, ΔE_s is the steady-state voltage change after removing the current pulse, ΔE_τ is the voltage change during the current pulse (excluding the IR drop), and τ is the duration of the current pulse[23]. A larger value of log D indicates a faster lithium-ion diffusion rate within the material. Figure 3F presents the lithium-ion diffusion rates in the anodes. Evidently, the average log D for the Si/CNFs/C anode is -12.672, significantly higher than that of the Si/CNFs anode (-12.829) and the Si/C anode (-13.172). Compared to Si/C, the Si/CNFs anode exhibits better lithium-ion diffusion rates due to the presence of CNFs, which provide one-dimensional ion transport channels, enhancing ion mobility within the composite[24]. Furthermore, the introduction of CQDs-C in the Si/CNFs/C anode forms a highly interconnected 3D ion transport network. The carbon layers derived in situ from CQDs on the inner walls of the Si pores reduce the diffusion distance for lithium ions and increase the active surface area, significantly enhancing lithium-ion diffusion and electrochemical kinetics compared to the Si/CNFs anode[25]. We also performed EIS measurements, as shown in Figure 3G. The carbon layers derived in situ from CQDs increase the conductivity of the Si particles. Interestingly, the Si/C anode shows the lowest impedance, possibly due to its simpler structure without additional conductive networks. The Si/CNFs/C anode exhibits the highest impedance, which may result from the dense and relatively thick carbon coating on its surface[26].

High-rate performance in lithium-ion batteries is enabled by anodes with significant pseudocapacitive contributions, reduced lithium-ion diffusion pathways, and efficient mass transport kinetics[27]. To probe the origin of the superior rate capability of the Si/CNFs/C anode, CV tests were performed at various scan rates (0.2 mV s^{-1}, 0.4 mV s^{-1}, 0.6 mV s^{-1}, 0.8 mV s^{-1}, and 1.0 mV s^{-1}) for all anodes, as shown in Supplementary Figure 5, to quantify their pseudocapacitive behavior[28]. The pseudocapacitive and diffusion-controlled contributions were separated using

$$i(\mathrm{v}) = \mathrm{k}_1 v + \mathrm{k}_2 v^{1/2} \quad (2)$$

where i represents the peak current, v indicates the scan rate, and k_1 and k_2 correspond to the surface-controlled (pseudocapacitive) and diffusion-controlled processes, respectively. As illustrated in Figure 3H-I and Supplementary Figure 6, at the same scan rate of 0.6 mV s^{-1}, the Si/CNFs/C anode exhibits the highest pseudocapacitive contribution of 83.1%. Furthermore, as the scan rate increases from 0.2 mV s^{-1} to 1.0 mV s^{-1}, the pseudocapacitive-controlled contribution for the Si/CNFs/C anode gradually increases from 69.1% to 91.8%. This enhanced pseudocapacitive effect effectively reduces polarization and energy loss, thereby enabling the Si/CNFs/C anode to maintain excellent electrochemical performance at high current densities[29].

To evaluate the long-term cycling stability of the three anodes, ultra-long cycling tests were conducted at a current density of 1 A g^{-1}, as depicted in Figure 4A. During the early cycles, all anodes experienced a slight capacity reduction, attributed to the initial lithiation of Si and minor structural volume changes. After 1,000 cycles, the Si/CNFs/C anode exhibited an impressive reversible capacity of 1,107.7 mAh g^{-1}, which is over three times higher than that of the Si/CNFs anode (365.3 mAh g^{-1}) and more than twice that of the Si/C anode (513 mAh g^{-1}). A comparative analysis of the cycling performance, shown in Figure 4B, reveals that the Si/CNFs/C anode outperforms a wide range of previously reported Si-based materials, demonstrating its exceptional stability and robust capacity retention over extended cycling.

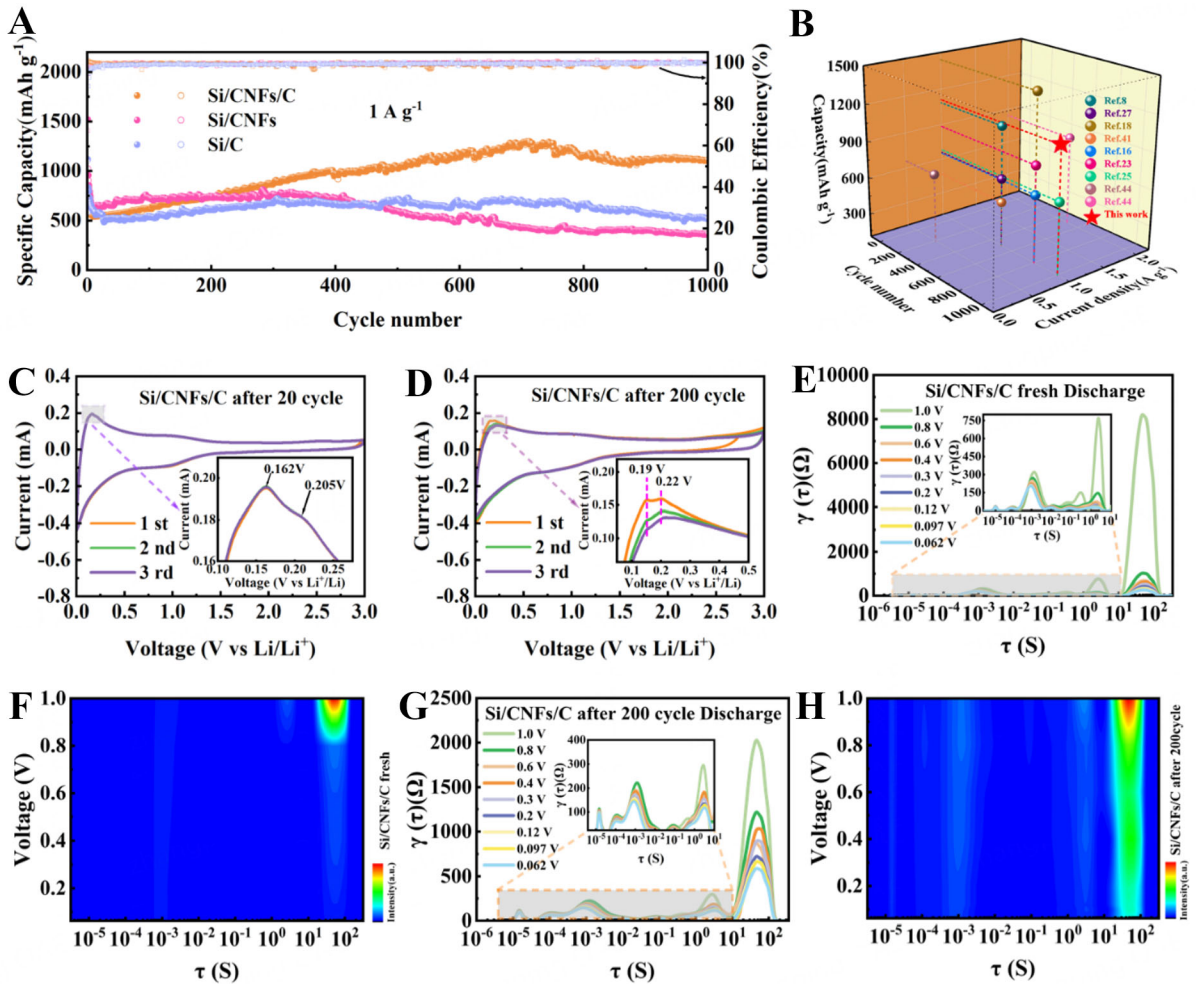

Figure 4. (A) Long-term cycling performance of Si/C, Si/CNFs, and Si/CNFs/C anodes at 1,000 mA g^{-1}; (B) Comparative analysis of cycling performance with previously reported studies. (C and D) CV curves of the Si/CNFs/C anode recorded after 20 and 200 cycles, respectively; (E-H) DRT curves and corresponding transformations of *in-situ* EIS spectra for the Si/CNFs/C anode in its fresh state and after 200 cycles of operation. CNFs: Carbon nanofibers; CV: cyclic voltammetry; DRT: distribution of relaxation times; EIS: electrochemical impedance spectroscopy.

Building upon the impressive long-term cycling performance of the Si/CNFs/C anode, we observed a particularly intriguing phenomenon: the anode's capacity not only stabilized but actually increased during prolonged cycling. Specifically, during the 200-cycle test at a current density of 0.1 A g^{-1}, the capacity of the Si/CNFs/C anode initially exhibited a slight decline but then began to increase steadily over subsequent cycles. This upward trend in capacity was evident across various current densities during the rate performance tests, and it became even more pronounced when the current density was returned to 0.1 A g^{-1} after high-rate cycling. Notably, during long-term cycling at a high current density of 1 A g^{-1}, the capacity increase became even more pronounced. This unexpected behavior immediately captured our attention, as capacity increases during cycling are uncommon and suggest unique underlying mechanisms. To delve deeper into this phenomenon, we conducted a series of electrochemical analyses to elucidate the reasons behind the capacity enhancement. Firstly, we performed CV tests on cells after 20 cycles, as shown in Figure 4C. Compared to the CV curve of the fresh cell, which displayed only a single oxidation peak, the anode cycled 20 times exhibited two characteristic Si oxidation peaks at 0.162 V and 0.205 V. This indicates the activation of additional Si active sites that were initially inaccessible. Furthermore, after 200 cycles, these

oxidation peaks became more pronounced and shifted to 0.19 V and 0.22 V [Figure 4D], suggesting that more Si particles embedded within the carbon matrix were gradually being activated and participating in the lithium storage process. Moreover, the reduced overlap among the CV curves near the oxidation peaks and around the reduction peak at 0.05 V implies that the activation process was still ongoing, contributing additional capacity in subsequent cycles[16]. This progressive activation of Si particles likely results from the gradual penetration of the electrolyte into the composite and the structural rearrangement of the anode during cycling, which facilitates better access of lithium ions to previously isolated Si domains[30].

To gain deeper insights into the intriguing capacity increase observed in the Si/CNFs/C anode during prolonged cycling, we conducted EIS measurements after different numbers of cycles, as illustrated in Supplementary Figure 7. The Nyquist plots exhibit two distinct semicircles in the medium-to-high frequency range and a straight line in the low-frequency region, offering insights into the anode's electrochemical behavior, with corresponding kinetic parameters detailed in Supplementary Table 1. The semicircle near the high-frequency region corresponds to the resistance of the SEI (R_{SEI}), while the second semicircle, located in the medium-frequency region, represents the R_{ct}[27]. As shown in Supplementary Figure 7B, after three cycles, the relatively high R_{SEI} suggests that the SEI layer is still forming and not yet fully stabilized, thereby hindering lithium-ion transport[31]. As cycling progresses to 50 cycles, we observe that R_{SEI} slightly decreases compared to the value after three cycles; this observed reduction in R_{SEI} suggests that the SEI layer is becoming more stable, with a more uniform chemical composition and physical structure, thus facilitating smoother lithium-ion passage[32]. However, at 100 cycles, R_{SEI} increases significantly to 16.7 Ω. This rise in resistance indicates changes occurring within the SEI layer; we interpret this increase as evidence that newly activated Si particles are beginning to participate in lithiation reactions, leading to uneven SEI growth or inhomogeneous reactions on the anode surface, which temporarily increase resistance[33]. By comparing R_{SEI} values at different cycles, we deduce that the state of the SEI layer is changing due to the activation of Si particles[34]. By 200 cycles, R_{SEI} dramatically decreases to 6.1 Ω, even lower than after 50 cycles. This significant reduction in R_{SEI} suggests that the chemical composition and structure of the SEI layer have further stabilized, enhancing lithium-ion transport within the anode and reducing resistance[35]. Similarly, the medium-frequency semicircle representing R_{ct} undergoes analogous transformations. After 50 cycles, R_{ct} decreases markedly compared to after three cycles, indicating improved conductive pathways and enhanced electron transfer kinetics; this suggests that the conductive network within the composite has become more efficient, facilitating charge transfer[36]. As cycling continues to 100 cycles, R_{ct} increases, which we interpret as resulting from newly activated mesoporous Si particles that have not yet established effective conductive pathways with the carbon matrix and the external electrolyte. By comparing R_{ct} data at different cycles, we deduce that the state of the conductive pathways is evolving[37]. By 200 cycles, R_{ct} diminishes again as these Si particles form robust connections with the carbon matrix and electrolyte, enhancing charge transfer[38]. To further substantiate these findings, we analyzed the Warburg coefficient (σ), derived from the relationship between the real part of the impedance (Z') and the inverse square root of angular frequency ($\omega^{-1/2}$), as depicted in Supplementary Figure 7C. The σ is inversely proportional to the D_{Li}^+; the trend of D_{Li}^+ mirrors the changes observed in R_{SEI} and R_{ct}, indicating that the activation and structural reconfiguration processes intricately affect not only the Si particles and conductive pathways but also the lithium-ion transport routes[23]. By comparing data at different cycles, we conclude that lithium-ion diffusion is influenced by these evolving processes. Collectively, these interwoven observations depict a dynamic system where continuous activation of Si particles drives structural evolution. Using the impedance data at different cycling stages, we infer that initially, the activation introduces transient impedances, but over time, the system reorganizes into a more efficient architecture. This progression leads to stabilized SEI layers, re-establishes conductive networks, and enhances lithium-ion transport, thereby explaining the remarkable capacity increase during cycling.

To gain deeper insights into the internal electrochemical processes occurring within the Si/CNFs/C anode during cycling, we employed the *in-situ* DRT technique. We chose DRT because it allows us to decompose the impedance spectra into individual electrochemical processes without relying on equivalent circuit models, thereby providing an unbiased and detailed assessment of the anode's dynamic behavior[39]. This approach not only avoids the potential pitfall of using results to prove results but also offers a deeper understanding of the mechanisms at play, directly connecting this analysis with our earlier observations of capacity enhancement and impedance changes. In the DRT spectra, as shown in Figure 4E-H and Supplementary Figure 8, three distinct peaks are identified, each corresponding to specific time intervals associated with different electrochemical processes: Peak (i) with time constants greater than 10 s (R_D: Diffusion Resistance) represents the diffusion of Li^+ ions within the bulk of the anode material (bulk diffusion), indicating the impedance associated with Li^+ ions penetrating into the material; Peak (ii) with time constants between 10^{-4} s and 10 s (R_{ct}) corresponds to the R_{ct} between the material surface and the bulk, reflecting the kinetics of electrochemical reactions at the anode/electrolyte interface; and Peak (iii) with time constants less than 10^{-4} s (R_{SEI}) is associated with interfacial reactions at the SEI layer, representing the impedance encountered by lithium ions traversing the SEI layer[40]. As for DRT results, more approximate time constants for different DRT peaks of the fresh Si/CNFs/C anode and after 200 cycles are provided in Supplementary Tables 2 and 3, respectively[41]. By comparing the fresh anode with the one after 200 cycles, we observed that the R_D and R_{ct} values in the cycled anode are significantly lower. This reduction indicates that after prolonged cycling, the Si/CNFs/C anode exhibits faster electron and ion transport due to the activation of Si particles and the establishment of efficient conductive networks. Notably, the reduction in R_D suggests that previously inactive Si sites have become electrochemically active, facilitating improved lithium-ion diffusion within the bulk material, which directly supports our earlier conclusion that Si activation contributes to the capacity increase. The voltage range of 0.8 V to 1.0 V is critical for SEI film formation; in the fresh cell, the R_{ct} and R_D peaks within this voltage range increase sharply due to substantial SEI layer formation resulting from initial reactions on the fresh Si surface. Conversely, in the anode after 200 cycles, the impedance in this region shows only a slight increase, suggesting that during cycling, only a small portion of Si becomes activated and contributes to SEI formation, aligning with our previous conclusions regarding the gradual activation of Si particles and providing additional evidence linking the activation process to changes in electrochemical performance. Furthermore, the contour plots reveal that in the fresh cell, the bulk diffusion impedance associated with SEI formation is relatively large, indicating that the initial formation of the SEI layer and inactive Si particles hinder lithium-ion diffusion within the anode; in contrast, for the anode after 200 cycles, the bulk impedance remains relatively uniform throughout the discharge process, demonstrating that the anode has developed efficient ion transport pathways. This uniformity explains why the Si/CNFs/C anode exhibits the highest impedance in the EIS data of the fresh cell, as the initial high impedance is attributed to the large bulk resistance from inactive Si particles and substantial SEI formation. By utilizing DRT analysis, we provide a comprehensive and independent evaluation of the internal electrochemical processes, effectively linking our earlier macroscopic observations to microscopic mechanisms. The detailed insights into the time constants associated with different electrochemical processes and their evolution during cycling not only corroborate our hypothesis about Si activation but also explain the initial high impedance observed in the fresh anode.

The structural evolution of Si/C, Si/CNFs, and Si/CNFs/C anodes after 1,000 cycles was investigated via SEM, as shown in Figure 5A-F, providing critical insights into the volume changes of these composite Si anodes. Initially, the anode thicknesses were measured to be 8.5 μm, 11.2 μm, and 11.1 μm for Si/CNFs/C, Si/CNFs, and Si/C, respectively. After 1,000 cycles, these values increased to 10 μm, 25.2 μm, and 14.1 μm, corresponding to expansions of 17.6%, 123.2%, and 27.2%, respectively. Notably, the Si/CNFs/C anode demonstrated the lowest volume expansion, a testament to its robust and innovative structural design. The CQDs-C forms a conformal coating around Si particles, effectively restraining their volumetric expansion

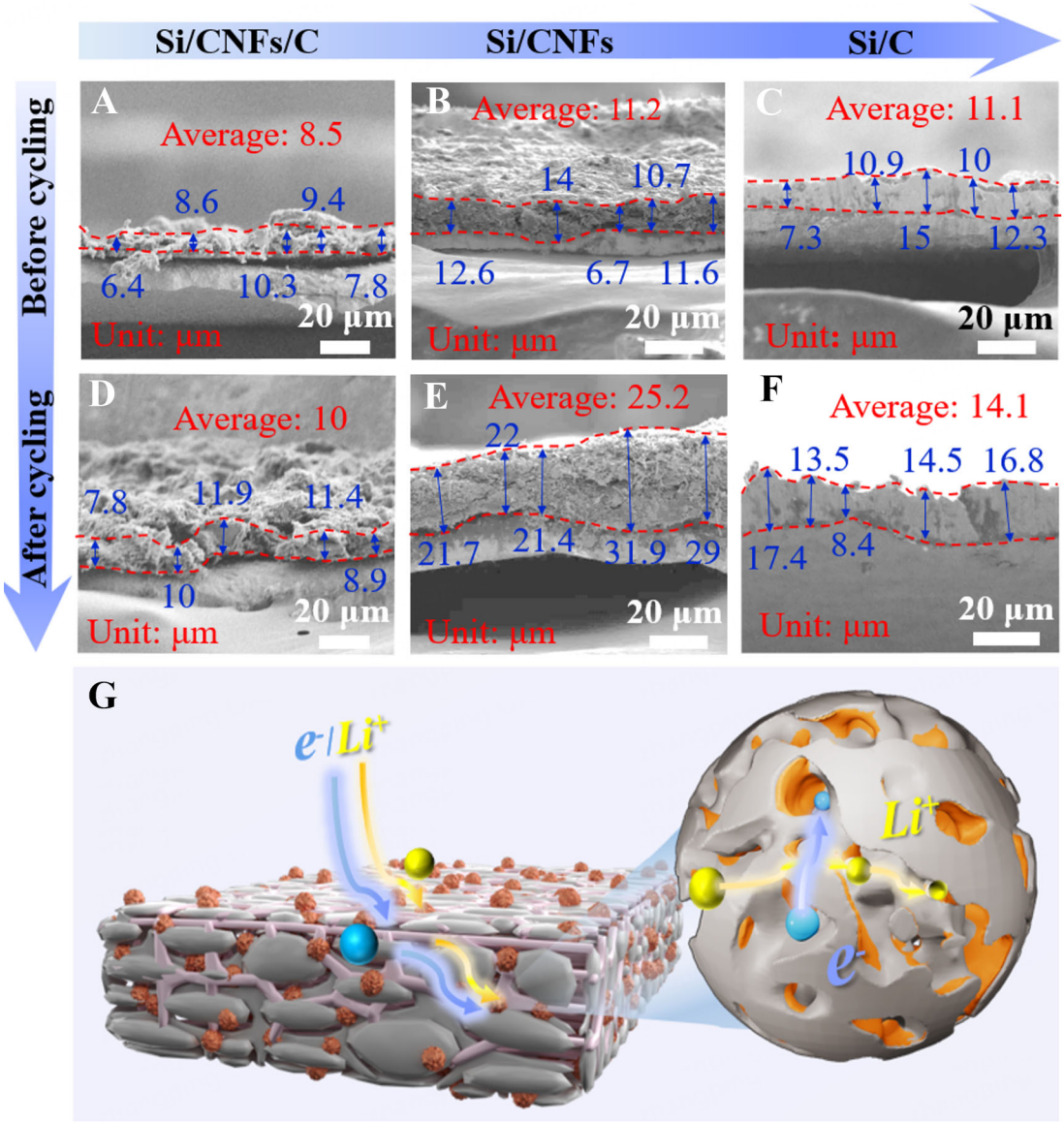

Figure 5. Cross-sectional images of anodes before cycling: (A) Si/CNFs/C, (B) Si/CNFs, (C) Si/C. After 1,000 cycles: (D) Si/CNFs/C, (E) Si/CNFs; (F) Si/C; (G) Schematic of ion and electron transport pathways in the composite structure. CNFs: Carbon nanofibers.

during repeated lithiation and delithiation cycles[42]. Simultaneously, CNFs function as a mechanically resilient framework, accommodating the stress induced by the inherent volume changes of Si and maintaining the structural integrity of the electrode during prolonged cycling[43].

Beyond mechanical stability, the 3D architecture of the Si/CNFs/C anode delivers substantial enhancements in both electron and lithium-ion transport, as illustrated in Figure 5G. The interconnected CNF network ensures efficient electron conduction, enabling uniform charge distribution throughout the anode. Concurrently, the *in-situ* carbon layers derived from CQDs-C not only immobilize the Si particles but also establish well-dispersed ion diffusion pathways, fostering uniform and rapid lithium-ion transport. These synergistic effects mitigate lithium-ion concentration polarization, alleviate localized stress, and promote uniform lithiation and delithiation processes. This unique structural configuration effectively reduces internal resistance, supports high-rate capability, and enhances cycling stability.

To gain a deeper understanding of the fundamental reasons behind the improvement afforded by carbon coating on Si-based materials, we performed DFT calculations on Si/CNFs/C[44]. As illustrated in Supplementary Figure 9, in the Si/CNFs/C model, the blue spherical structures represent the crystalline Si substrate, while the red spheres denote oxygen atoms. The combination of Si and oxygen atoms indicates the small amount of SiO_2 formed by surface oxidation of Si, as revealed by the XPS analysis. The brown layer on top is the carbon coating, which consists of amorphous carbon derived from CNFs and CQDs-C. Figure 6A shows the differential charge density distribution at the Si(111)/C(001) interface, illustrating how charges are redistributed at this interface and providing crucial information on the interaction between the Si(111) and C(001) surfaces. First, the differential charge density in the Si(111) region is close to zero, indicating that the charge distribution on the Si surface remains relatively stable. However, in the C(001) region, the differential charge density undergoes a pronounced change, particularly at the interface (~15 Å). The sharp peaks observed in this area reveal significant charge accumulation or depletion. This phenomenon can be attributed to the electronic interaction between the two materials, where the carbon layer draws electrons from the Si surface, causing a marked change in the surface charge density of carbon. Such electron transfer implies a strong electronic coupling effect at the Si/CNFs/C interface, exerting a significant influence on the electronic states of the Si surface[45]. The change in charge density directly reflects the interfacial interaction of these materials, further demonstrating that the Si layer can effectively modify the electronic structure of the Si surface through electron transfer, potentially impacting the interface's conductivity, stability, and electrochemical performance. Figure 6B presents the planar-averaged potential distribution of the Si/CNFs/C sample along the distance axis, with dashed lines marking key energy levels, including the Fermi level (E_F) and the vacuum level (E_{vac}). From these calculations, the work function (WF) is found to be 4.82 eV, representing the minimum energy required for electrons to escape from the material's surface. The WF is closely tied to the surface structure of the material[46]. In the Si/CNFs/C composite, the conductive network formed by CQDs-C and CNFs on the Si surface significantly modulates the surface energy level distribution, thereby creating a surface barrier that facilitates both electron release and transport.

Figure 6C and D provides a detailed view of the differential charge density distribution at the Si and C interface, represented using isosurface plots with color gradients distinguishing regions of charge accumulation and depletion. The yellow regions indicate charge accumulation, while the cyan-blue regions represent charge depletion. It is clearly observed that a large yellow cloud is present on the side near the carbon layer, while a distinct cyan-blue region is observed in the adjacent area of the Si surface. This indicates significant electron transfer at the interface, where electrons flow from the Si substrate to the carbon layer. This electron coupling at the interface is the essential mechanism through which carbon coating improves the performance of Si-based materials. First, the migration of electrons from the Si surface to the carbon layer effectively passivates the Si surface states, reducing the interface defect density and minimizing the likelihood of side reactions. In lithium-ion batteries, this passivation can significantly enhance the chemical stability and cycling life of the material. Second, the conductive network formed by the carbon layer enhances the efficiency of electron transport, making the charge distribution at the interface more balanced and reducing interface impedance, which is particularly critical for achieving high-rate charge and discharge performance[47]. Additionally, the strong interface bonding between the carbon coating and the Si surface partially buffers the volume expansion of Si during charge and discharge, thereby reducing issues such as particle pulverization and interface delamination. These intuitive differential charge density distributions in the figure confirm that the carbon layer not only protects the Si surface through chemical bonding but also reconstructs the interface environment in terms of electronic structure, providing an important foundation for the stable and efficient operation of Si-based materials in lithium-ion batteries.

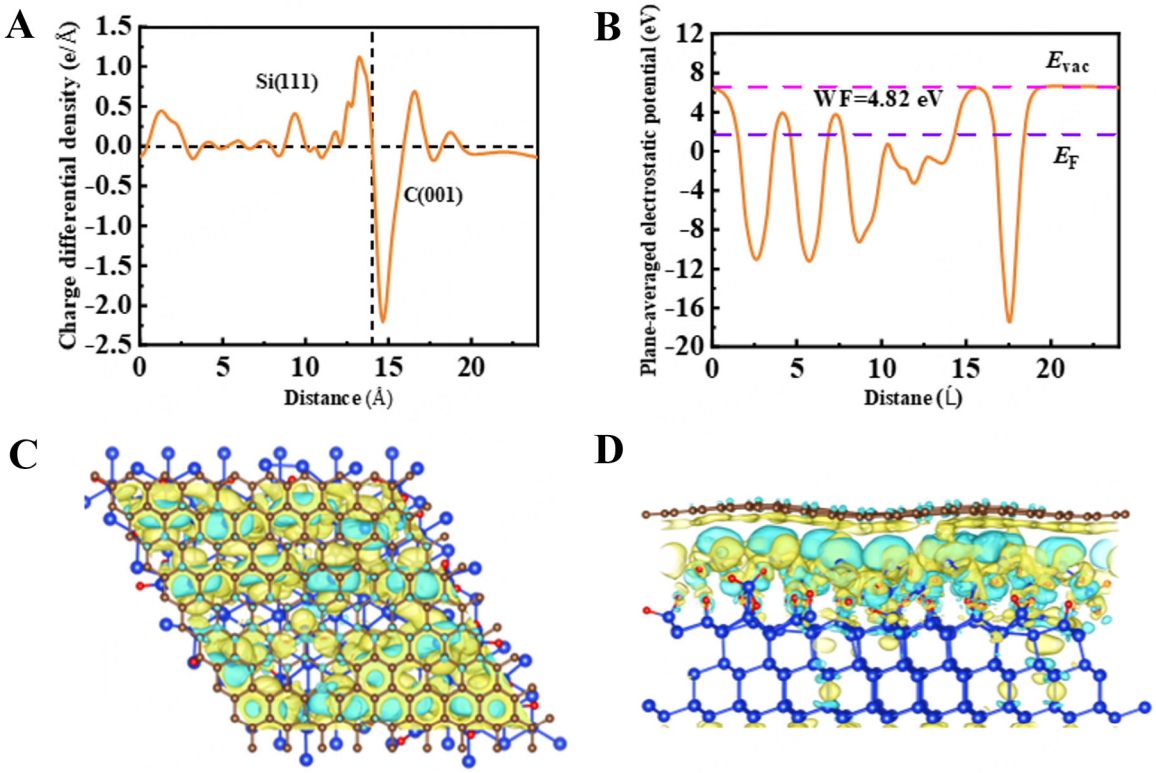

Figure 6. (A) One-dimensional difference charge density profile along the interface; (B) Work Function of the Composite Interface; (C) Top view of the three-dimensional difference charge density isosurface; (D) Side view of the three-dimensional difference charge density isosurface. WF: Work function.

CONCLUSIONS

In this study, we have successfully designed and synthesized a 3D Si/CNFs/C anode. The innovative architecture enhances electron and ion transport, mitigates the volume expansion of Si during cycling, and ensures mechanical stability. Consequently, the Si/CNFs/C anode has delivered excellent electrochemical performance, achieving a reversible capacity of 1,172.4 mAh g^{-1} after 200 cycles at 0.1 A g^{-1} and maintaining 1,107.7 mAh g^{-1} after 1,000 cycles at 1 A g^{-1}. Notably, a unique capacity increase phenomenon has been observed during prolonged cycling, which has been attributed to the progressive activation of Si particles deeply embedded within the composite matrix. We revealed that this activation process is accompanied by dynamic structural and electrochemical adjustments, including the formation of efficient conductive pathways and stabilized SEI layers. These findings underscore the self-improving behaviors of the Si/CNFs/C anode, providing new insights into designing Si-based anodes with gradual activation mechanisms to enhance cycling stability and high-rate performance. Overall, this work addresses the critical challenges of Si anodes and details the mechanism responsible for the capacity increase observed during cycling, offering a robust framework for the development of high-performance Si-based anodes for next-generation lithium-ion batteries.

DECLARATIONS

Authors' contributions

Writing - original draft, methodology, investigation, conceptualization: Liu, J.
Writing - original draft, investigation, formal analysis: Wan, Y.

Investigation: Wang, K.; Wang, K.
Writing - review and editing, formal analysis: Sun, W.
Investigation, conceptualization: Dai, J.
Investigation, formal analysis: Li, Z.
Writing - review and editing, investigation, formal analysis: Ran, F.

Availability of data and materials

The data supporting the findings of this study are available within this Article and its Supplementary Materials. Further data are available from the corresponding authors upon request.

Financial support and sponsorship

This work was financially supported by the National Natural Science Foundation of China (22369009), the Gansu Provincial Youth Science and Technology Fund Projects (23JRRA865, 24JRRA989), the Science and Technology Plan Project of Jinchang (2024GY004), the Natural Science and Technology Development Guidance Plan Fund Project of Lanzhou (2022-ZD-149), the Gansu Provincial Natural Science Foundation Project (24JRRF006), the Gansu Provincial Youth Talent Team Project (2024QNTD38), the Jiuquan Science and Technology Support Plan Project (2023CA2057), the Gansu Provincial University Teachers Innovation Fund Project (2025A-043), and the Tianyou Youth Talent Lift Program of Lanzhou Jiaotong University.

Conflicts of interest

All authors declared that there are no conflicts of interest.

Ethical approval and consent to participate

Not applicable.

Consent for publication

Not applicable.

REFERENCES

1. He, Z.; Zhang, C.; Zhu, Y.; Wei, F. The acupuncture effect of carbon nanotubes induced by the volume expansion of silicon-based anodes. *Energy. Environ. Sci.* **2024**, *17*, 3358-64. DOI
2. Liu, J.; Huang, L.; Wang, H.; et al. The origin, characterization, and precise design and regulation of diverse hard carbon structures for targeted applications in lithium-/sodium-/potassium-ion batteries. *Electrochem. Energy. Rev.* **2024**, *7*, 34. DOI
3. Zhang, P.; Wang, X.; Zhang, Y.; et al. Burgeoning silicon/MXene nanocomposites for lithium ion batteries: a review. *Adv. Funct. Mater.* **2024**, *34*, 2402307. DOI
4. He, Z.; Zhang, C.; Zhu, Z.; Yu, Y.; Zheng, C.; Wei, F. Advances in carbon nanotubes and carbon coatings as conductive networks in silicon-based anodes. *Adv. Funct. Mater.* **2024**, *34*, 2408285. DOI
5. Wang, L.; Han, J.; Kong, D.; Tao, Y.; Yang, Q. H. Enhanced roles of carbon architectures in high-performance lithium-ion batteries. *Nano-Micro. Lett.* **2019**, *11*, 5. DOI PubMed PMC
6. Yan, W.; Mu, Z.; Wang, Z.; et al. Hard-carbon-stabilized Li-Si anodes for high-performance all-solid-state Li-ion batteries. *Nat. Energy.* **2023**, *8*, 800-13. DOI
7. Zhou, J.; Lu, Y.; Yang, L.; et al. Sustainable silicon anodes facilitated via a double-layer interface engineering: inner SiO*x* combined with outer nitrogen and boron co-doped carbon. *Carbon. Energy.* **2022**, *4*, 399-410. DOI
8. Han, M.; Mu, Y.; Wei, L.; Zeng, L.; Zhao, T. Multilevel carbon architecture of subnanoscopic silicon for fast-charging high-energy-density lithium-ion batteries. *Carbon. Energy.* **2024**, *6*, e377. DOI
9. Li, W.; Xu, Y.; Wang, G.; Xu, T.; Si, C. Design and functionalization of lignocellulose-derived silicon-carbon composites for rechargeable batteries. *Adv. Energy. Mater.* **2024**, *14*, 2403593. DOI
10. Cheng, Z.; Jiang, H.; Zhang, X.; Cheng, F.; Wu, M.; Zhang, H. Fundamental understanding and facing challenges in structural design of porous Si-based anodes for lithium-ion batteries. *Adv. Funct. Mater.* **2023**, *33*, 2301109. DOI

11. Zhao, H.; Li, J.; Zhao, Q.; et al. Si-based anodes: advances and challenges in Li-ion batteries for enhanced stability. *Electrochem. Energy. Rev.* **2024**, *7*, 11. DOI
12. Zhang, Z.; Chen, Y.; Sun, S.; et al. Recent progress on three-dimensional nanoarchitecture anode materials for lithium/sodium storage. *J. Mater. Sci. Technol.* **2022**, *119*, 167-81. DOI
13. Liu, J.; Di, Z.; Wan, Y.; et al. Sub-micron porous Si-C/graphite anode with interpenetrated 3D conductive networks towards high-performance lithium-ion batteries. *J. Alloys. Compd.* **2024**, *983*, 173930. DOI
14. Wang, D.; Wang, Q.; Tan, M.; et al. Biomass CQDs derivate carbon as high-performance anode for K-ion battery. *J. Alloys. Compd.* **2022**, *922*, 166260. DOI
15. Ha, T.; Reddy, B.; Ryu, H.; et al. A study on the electrochemical properties of silicon/carbon composite for lithium-ion battery. *J. Energy. Storage.* **2023**, *63*, 107045. DOI
16. Yan, J.; Gao, C.; Qi, S.; et al. Encapsulation of nano-Si into MOF glass to enhance lithium-ion battery anode performances. *Nano. Energy.* **2022**, *103*, 107779. DOI
17. Zhang, R.; Jia, F.; Sun, C.; et al. Enhanced lithium storage performance: dual-modified electrospun Si@MnO@CNFs composites for advanced anodes. *ACS. Appl. Mater. Interfaces.* **2024**, *16*, 38028-40. DOI
18. Zeng, K.; Li, T.; Qin, X.; et al. A combination of hierarchical pore and buffering layer construction for ultrastable nanocluster Si/SiO_x anode. *Nano. Res.* **2020**, *13*, 2987-93. DOI
19. Tong, Y.; Wu, Y.; Liu, Z.; Yin, Y.; Sun, Y.; Li, H. Fabricating multi-porous carbon anode with remarkable initial coulombic efficiency and enhanced rate capability for sodium-ion batteries. *Chin. Chem. Lett.* **2023**, *34*, 107443. DOI
20. Song, L.; Peng, C.; Yang, F.; Wang, L.; Jiang, Y.; Wang, Y. Surface spatial confinement effect on Mn-Co LDH@carbon dots for high-performance supercapacitors. *ACS. Appl. Energy. Mater.* **2021**, *4*, 4654-61. DOI
21. Zuo, X.; Wang, X.; Xia, Y.; et al. Silicon/carbon lithium-ion battery anode with 3D hierarchical macro-/mesoporous silicon network: self-templating synthesis via magnesiothermic reduction of silica/carbon composite. *J. Power. Sources.* **2019**, *412*, 93-104. DOI
22. Zhu, R.; Wang, Z.; Hu, X.; Liu, X.; Wang, H. Silicon in Hollow carbon nanospheres assembled microspheres cross-linked with n-doped carbon fibers toward a binder free, high performance, and flexible anode for lithium-ion batteries. *Adv. Funct. Mater.* **2021**, *31*, 2101487. DOI
23. Fan, X.; Cai, T.; Wang, S.; Yang, Z.; Zhang, W. Carbon nanotube-reinforced dual carbon stress-buffering for highly stable silicon anode material in lithium-ion battery. *Small* **2023**, *19*, 2300431. DOI
24. Wang, S.; Zhang, J.; Zhang, L.; et al. 3D self-supporting core-shell silicon-carbon nanofibers-based host enables confined Li^+ deposition for lithium metal battery. *Nano. Energy.* **2024**, *131*, 110255. DOI
25. He, Z.; Xiao, Z.; Yue, H.; et al. Single-walled carbon nanotube film as an efficient conductive network for Si-based anodes. *Adv. Funct. Mater.* **2023**, *33*, 2300094. DOI
26. Araño, K. G.; Yang, G.; Armstrong, B. L.; et al. Carbon coating influence on the formation of percolating electrode networks for silicon anodes. *ACS. Appl. Energy. Mater.* **2023**, *6*, 11308-21. DOI
27. Gao, Y.; Song, S.; He, F.; et al. Controllable synthesis of hollow dodecahedral Si@C core-shell structures for ultrastable lithium-ion batteries. *Small* **2024**, *20*, 2406489. DOI
28. Niu, Y.; Wei, M.; Xi, F.; et al. Preparation of WSi@SiOx/Ti3C2 from photovoltaic silicon waste as high-performance anode materials for lithium-ion batteries. *iScience* **2024**, *27*, 110714. DOI
29. Jiang, Y.; Liu, J. Definitions of pseudocapacitive materials: a brief review. *Energy. Environ. Mater.* **2019**, *2*, 30-7. DOI
30. Huo, H.; Jiang, M.; Bai, Y.; et al. Chemo-mechanical failure mechanisms of the silicon anode in solid-state batteries. *Nat. Mater.* **2024**, *23*, 543-51. DOI
31. Surace, Y.; Leanza, D.; Mirolo, M.; et al. Evidence for stepwise formation of solid electrolyte interphase in a Li-ion battery. *Energy. Storage. Mater.* **2022**, *44*, 156-67. DOI
32. Zhang, R.; Yu, P.; Li, Z.; Shen, X.; Yu, Y.; Yu, J. Hierarchical porous structured Si/C anode material for lithium-ion batteries by dual encapsulating layers for enhanced lithium-ion and electron transports rates. *Small* **2025**, *21*, 2407276. DOI
33. He, Y.; Jiang, L.; Chen, T.; et al. Progressive growth of the solid-electrolyte interphase towards the Si anode interior causes capacity fading. *Nat. Nanotechnol.* **2021**, *16*, 1113-20. DOI
34. Wu, J.; Ihsan-ul-haq, M.; Chen, Y.; Kim, J. Understanding solid electrolyte interphases: advanced characterization techniques and theoretical simulations. *Nano. Energy.* **2021**, *89*, 106489. DOI
35. Qian, G.; Li, Y.; Chen, H.; et al. Revealing the aging process of solid electrolyte interphase on SiO_x anode. *Nat. Commun.* **2023**, *14*, 6048. DOI PubMed PMC
36. Geng, S.; Zhou, J.; Tan, B.; Zheng, B.; Zhang, K. Impact of thickness and charge rate on the electrochemical performance of Si-based electrodes. *Cell. Rep. Phys. Sci.* **2024**, *5*, 102305. DOI
37. Gaberšček, M. Understanding Li-based battery materials via electrochemical impedance spectroscopy. *Nat. Commun.* **2021**, *12*, 6513. DOI PubMed PMC
38. Shi, Y.; Wan, J.; Li, J.; et al. Elucidating the interfacial evolution and anisotropic dynamics on silicon anodes in lithium-ion batteries. *Nano. Energy.* **2019**, *61*, 304-10. DOI
39. Pan, K.; Zou, F.; Canova, M.; Zhu, Y.; Kim, J. Comprehensive electrochemical impedance spectroscopy study of Si-based anodes using distribution of relaxation times analysis. *J. Power. Sources.* **2020**, *479*, 229083. DOI
40. Li, H.; Yao, B.; Li, M.; et al. Three-dimensional carbon nanotubes buffering interfacial stress of the silicon/carbon anodes for long-

cycle lithium storage. *ACS. Appl. Mater. Interfaces.* **2024**, *16*, 53665-74. DOI

41. Zhang, W.; Chen, R.; Dai, Y.; et al. Asymmetric acceptor-donor small organic molecule enabling versatile and highly-stable aqueous zinc batteries. *Mater. Today.* **2024**, *78*, 32-45. DOI
42. Gao, J.; Zuo, S.; Liu, H.; et al. An interconnected and scalable hollow Si-C nanospheres/graphite composite for high-performance lithium-ion batteries. *J. Colloid. Interface. Sci.* **2022**, *624*, 555-63. DOI
43. Di, F.; Wang, Z.; Ge, C.; et al. Hierarchical pomegranate-structure design enables stress management for volume release of Si anode. *J. Mater. Sci. Technol.* **2023**, *157*, 1-10. DOI
44. Wang, V.; Xu, N.; Liu, J. C.; et al. VASPKIT: a user-friendly interface facilitating high-throughput computing and analysis using VASP code. *Comput. Phys. Commun.* **2021**, *267*, 108033. DOI
45. Kansara, S.; Kang, H.; Ryu, S.; Sun, H. H.; Hwang, J. Basic guidelines of first-principles calculations for suitable selection of electrochemical Li storage materials: a review. *J. Mater. Chem. A.* **2023**, *11*, 24482-518. DOI
46. Marri, I.; Amato, M.; Bertocchi, M.; et al. Surface chemistry effects on work function, ionization potential and electronic affinity of Si (100), Ge (100) surfaces and SiGe heterostructures. *Phys. Chem. Chem. Phys.* **2020**, *22*, 25593-605. DOI
47. Liu, Q.; Ji, Y.; Yin, X.; et al. Magnesiothermic reduction improved route to high-yield synthesis of interconnected porous Si@C networks anode of lithium ions batteries. *Energy. Storage. Mater.* **2022**, *46*, 384-93. DOI